International Journal of Nanomedicine

Dovepress

open access to scientific and medical research

Open Access Full Text Article

ORIGINAL RESEARCH

Synthetic Antibacterial Quaternary Phosphorus Salts Promote Methicillin-Resistant *Staphylococcus aureus*-Infected Wound Healing

Liang-Wen Shi[1,*], Quan-Quan Zhuang[2,*], Tai-Qin Wang[1], Xian-Dong Jiang[3], Yue Liu[4], Jing-Wen Deng[1], Huan-Huan Sun[5], Yi Li[4], Hao-Hong Li[4], Ting-Bo Liu[6], Jian-Zhi Liu[1]

[1]Department of Otorhinolaryngology, Fujian Medical University Union Hospital, Fuzhou, Fujian, People's Republic of China; [2]Department of Pharmacy, Affiliated Quanzhou First Hospital of Fujian Medical University, Quanzhou, Fujian, People's Republic of China; [3]Department of laboratory medicine, the School of Medical Technology and Engineering, Fujian Medical University, Fuzhou, Fujian, People's Republic of China; [4]College of Chemistry, Fuzhou University, Fuzhou, Fujian, People's Republic of China; [5]Department of Otolaryngology, Changji Region Hospital of Traditional Chinese Medicine, Changji, Xinjiang, People's Republic of China; [6]Fujian Institute of Hematology, Fujian Provincial Key Laboratory of Hematology, Fujian Medical University Union Hospital, Fuzhou, Fujian, People's Republic of China

*These authors contributed equally to this work

Correspondence: Jian-Zhi Liu, Department of Otorhinolaryngology, Fujian Medical University Union Hospital, Fuzhou, Fujian, People's Republic of China, Tel/Fax +86-591 83346181, Email liujianzhient@163.com; Ting-Bo Liu, Fujian Institute of Hematology, Fujian Provincial Key Laboratory of Hematology, Fujian Medical University Union Hospital, Fuzhou, Fujian, People's Republic of China, Tel/Fax +86-591 83357896, Email liutingboblood@163.com

Background: Drug-resistant microbes pose a global health concern, requiring the urgent development of effective antibacterial agents and strategies in clinical practice. Therefore, there is an urgent need to explore novel antibacterial materials to effectively eliminate bacteria. The synthesis of quaternary phosphonium salt in haloargentate systems, wherein the phosphorus atom is represented in a cationic form, is a possible strategy for the development of antibacterial materials.

Methods: Using (triphenyl)phosphonium-based quaternary phosphorus salts with different spacer lengths (n=2, 4, 6) as a template, we designed three kinds of quaternary phosphorus salts as effective antibacterial agents against drug-resistant bacteria.

Results: The synthesized quaternary phosphorus salt of (1,4-DBTPP)Br_2 effectively prevented the formation of the bacterial biofilms, and degraded bacterial membranes and cell walls by promoting the production of reactive oxygen species, which exhibited effective therapeutic effects in a rat model of a superficial wound infected with methicillin-resistant *Staphylococcus aureus*.

Conclusion: The quaternary phosphorus salt (1,4-DBTPP)Br_2 demonstrated hemocompatibility and low toxicity, revealing its potential in the treatment of clinical infections.

Keywords: quaternary phosphorus salts, reactive oxygen species, antibacterial, biocompatible, wound infection therapy

Introduction

The abuse of antibiotics has led to an increase in drug-resistant bacterial strains, posing significant international concern and accounting for more than 700,000 deaths yearly. This number is expected to increase to 10 million deaths by 2050, resulting in an economic loss of approximately 100 trillion USD.[1] Unfortunately, the development of novel antibiotics is challenging owing to the rapid emergence of resistant microorganisms. In addition, the development of novel antibacterial agents requires significant economic, time investments, as well as labor supply.[2]

Metal-based antibacterial therapeutics, such as gold nanoparticles,[3] silver nanoparticles,[4,5] copper-containing titanium alloy,[6] ZnO nanoparticles,[7] and iron oxide nanoparticles,[8] have attracted increasing attention owing to their excellent antibacterial activities, no-resistance cases, transport convenience, and higher efficiency,[9,10] However, the metabolism of metal ions in the body is extremely difficult, and the accumulation of metal ions has toxic side effects on the human body. Hence, the wide application of metal-containing antibacterial materials is limited.[11] In addition, the photothermal and photocatalytic property confers several metal-organic frameworks of nanomaterials with bactericidal effects on the

Received: 22 November 2022
Accepted: 21 February 2023
Published: 7 March 2023

Graphical Abstract

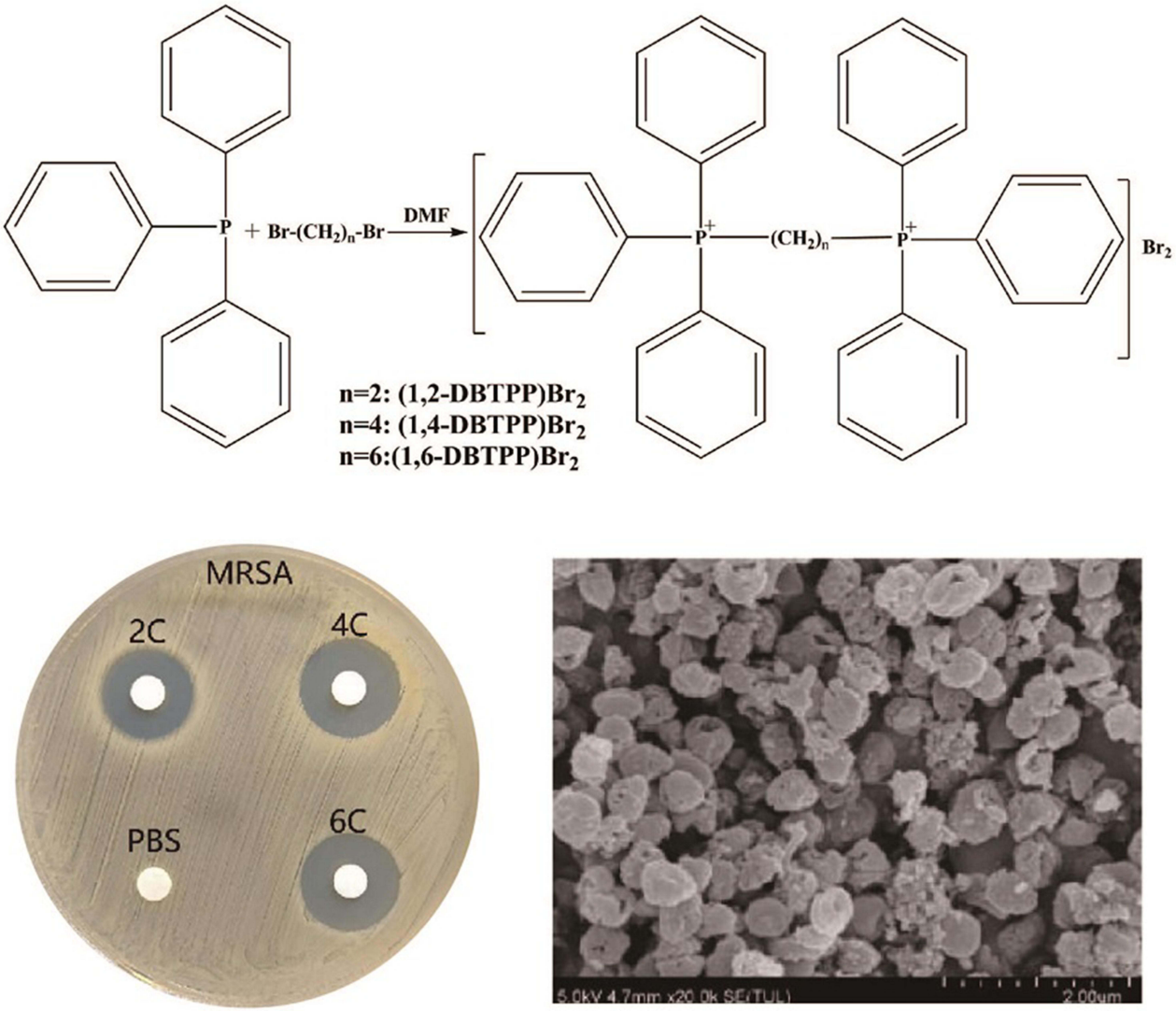

therapy for bacteria-infected wound healing.[12–15] Nevertheless, the antibacterial effects of these substances are considerably limited without light exposure.

The ideal antibacterial material for medical applications should exhibit efficient antimicrobial property and high selectivity towards bacterial cells, and low toxicity over mammalian cells.[16] Researchers have devoted considerable efforts to combat resistant bacterial infections, as shown by the continuous and extensive exploration of antibacterial peptides and cationic polymers.[17,18] Yang et al reported that Gram-negative bacteria could be disintegrated by an antimicrobial peptide with cationic and amphiphilic structures, which can insert into their cell surfaces.[19] Deber et al reported a novel cationic antimicrobial peptide with high selectivity for bacterial membranes and low toxicity towards mammalian membranes.[20] Antibacterial peptides have a low propensity to develop resistance; however, antimicrobial peptides have also suffered from poor antibacterial activity and high hemolysis in vivo, salt instability, as well as high cost, which highly limit their clinical implementation.[21] Moreover, quaternary ammonium and phosphonium salts have been designed and synthesized based on antibacterial peptides with cationic charge and amphiphilic structure. Cai et al

have developed amphiphilic quaternized β-chitin derivatives with biocompatible properties and antimicrobial activity for the treatment of wound healing.[22] Qi et al offered a facile one-pot strategy to construct quaternary ammonium chitosan hydrogels for treating diabetic wounds.[23,24] We have previously synthesized quaternary phosphorus/bromoargentate hybrids with good antibacterial properties, mediated by the inhibition of *S. mutans* and *C. albicans* growth. However, the antibacterial activity of these hybrids was limited by their poor solubility in neutral solutions.[25] Furthermore, the metal Ag may induce cytotoxicity in mammalian cells. Hence, the exploration of biodegradable antibacterial agents with excellent biocompatibility, low toxicity, and good solubility is highly needed for clinical applications.

In this study, we designed and successfully synthesized two alkyl-bis-(triphenyl) phosphonium bromides (1,2-DBTPP)Br_2, (1,4-DBTPP)Br_2, and (1,6-DBTPP)Br_2 in one step,[26] and evaluated their antibacterial activities against four pathogens using the minimum inhibitory concentration procedure. The results revealed that (1,4-DBTPP)Br_2 exhibited good solubility, low toxicity, and low hemolytic activity. Moreover, we investigated the effects of (1,4-DBTPP)Br_2 on the viability of bacteria, the formation of biofilm, and the recovery process of infected wounds in vivo (Scheme 1). Our results can help extend the biological applications of quaternary phosphonium salts.

Experimental Section

Preparation of Quaternary Phosphorus Salts

A facile one-step synthesis of triphenylphosphine with 1,2-dibromoethane was carried out to obtain two alkyl-bis-(triphenyl) phosphonium bromide (1, 2-DBTPP)Br_2, (1, 4-DBTPP)Br_2, and (1, 6-DBTPP)Br_2 in dimethylformamide (DMF) according to

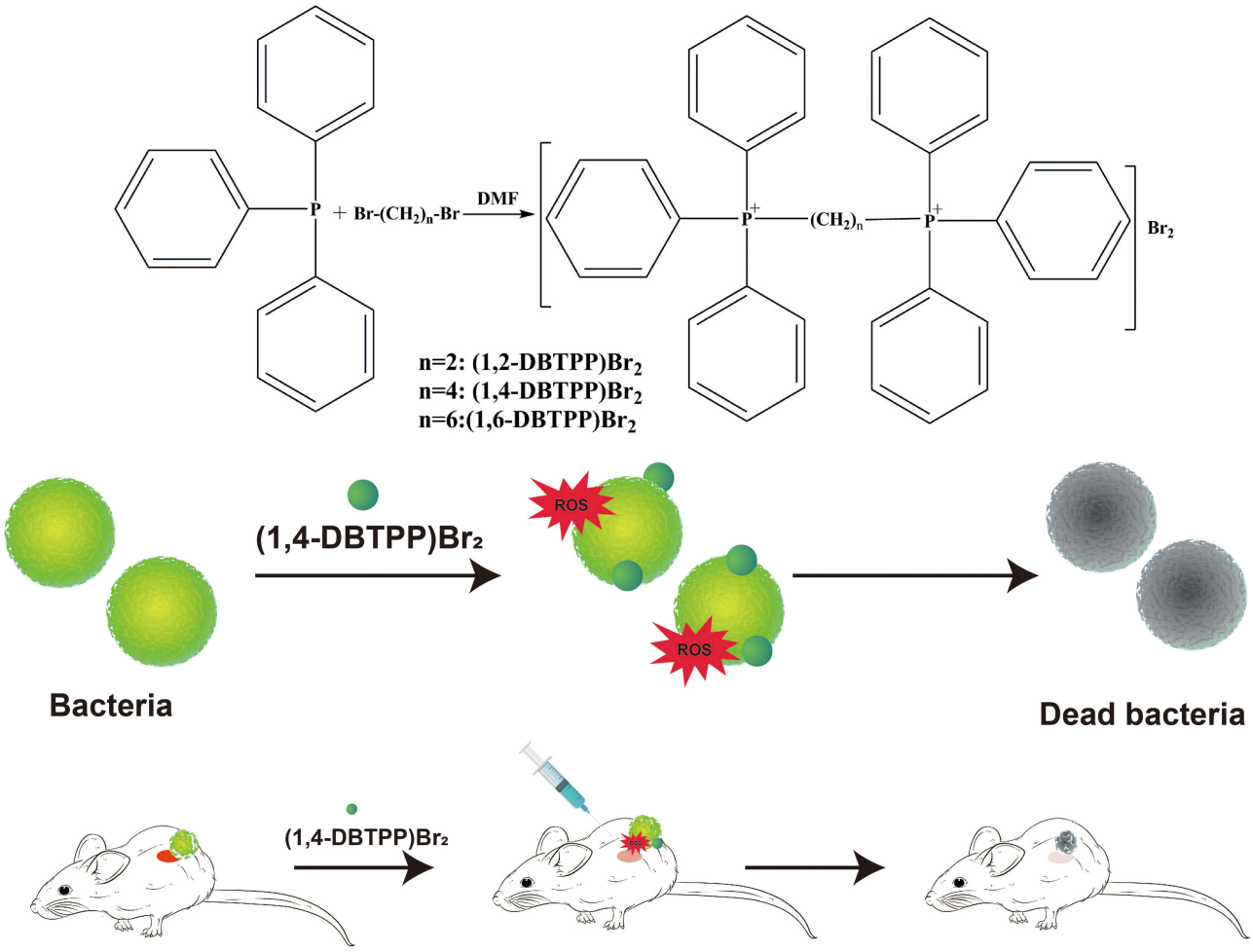

Scheme 1 Process of the synthesis of two alkyl-bis-(triphenyl)phosphonium bromides and schematic of the antibacterial mechanism of (1,4-DBTPP)Br_2.

a previously reported method.[27] Briefly, haloalkanes (10 mmoL) and Ph3P (30 mmoL) were dissolved in DMF (10 mL) and were reacted at 130 °C for 4 h. The mixtures were then cooled to room temperature, and the solvent was removed by rotation volatilization to extract the raw products, which were washed with n-hexane and dried in an oven.

Bacterial Culture

Bacterial strains stored at −80 °C were cultivated at 37 °C and maintained on blood agar plates for 24 h before use. MRSA cells were grown overnight on LB plates at 37 °C, harvested at the exponential growth phase via centrifugation, and then resuspended in a sterile 0.9% saline. MRSA cells were adjusted to a 0.5 McFarland standard (1.5×10^8 colony-forming unit [CFU] mL^{-1}) and then diluted to a concentration of 1.0×10^6 CFU mL^{-1} by 1:150 in Mueller Hinton Broth (MHB).

Bacterial Growth Curve and Time-Kill Studies

The assay was performed according to our previously validated method with minor changes.[27] Firstly, 180 μL of a MRSA cell suspension (1.0×10^6 CFU mL^{-1}) in LB broth medium was seeded in a 96-well plate, and different concentrations of (1,4-DBTPP)Br_2 (0−128 μg mL^{-1}) were added to each well. The growth curves of the MRSA cells were evaluated using an Automated Microbiology Analysis System (Bioscreen C, Turku, Finland) at 37 °C with shaking at 200 rpm. The optical density (OD_{600}) values were detected every 1 h for up to 30 h. Analysis of the time-kill curve was carried out by culturing MRSA strains in LB broth. Briefly, a 0.5 McFarland inoculum of MRSA was made in sterile saline solution (0.9% NaCl) from cultures grown on blood agar plates for 20 h at 35 °C. Three concentrations of (1,4-DBTPP)Br_2 in doubling dilutions ranging from 1 × minimum inhibitory concentrations (MIC) to 4 × MIC in 96-well microtiter plates were assessed. Ten microliters of one of the antimicrobial concentrations were added to each well, including ninety microliters of pre-incubated bacteria. At 0, 1, 2, 3, 4, 5, and 6 h after exposure, 100 μL aliquots of each dilution (1:10) were spread on LB agar plates and incubated at 35 °C for 20 h. Finally, the viable colonies were counted, and the time-kill curves of MRSA strains were constructed by plotting the survival rate versus the incubation time.[28]

Determination of Live/Dead Ratio Using Fluorescence Microscopy Imaging

The mixture of MRSA suspension (1.0×10^6 CFU mL^{-1}) and (1,4-DBTPP)Br_2 was seeded in 96-microtiter plates. After 24 h, the cells were washed with a sterile 0.9% saline by removing the planktonic suspension. The live and dead cells were visualized using a green-fluorescent membrane-permeant dye (SYTO 9) and a red-fluorescent damaged membrane-permeant dye (propidium iodide, PI), respectively, by fluorescence microscopy.

Observation of the Morphology and Bacterial Biofilm Using Scanning Electron Microscopy (SEM)

SEM was used to further observe bacterial morphology. Briefly, after incubation with 0 and 128 μg mL^{-1} of (1,4-DBTPP)Br_2 for 24 h, samples were washed thrice with sterile 0.9% saline, and the bacterial cells were harvested by centrifugation and fixed in glutaraldehyde (2.5%) for 2 h at 4 °C. Then, samples were washed using sterile 0.9% saline and dehydrated in a graded series of ethanol (30%, 50%, 70%, 80%, 85%, 90%, 95%, and 100%). The gold-sputter-coated specimens were observed using SEM (SU8020, Hitachi, Tokyo, Japan). To observe the bacterial biofilm, (1,4-DBTPP)Br_2 (32 μg mL^{-1}) and control samples were incubated with the MRSA solution (1.0×10^6 CFU mL^{-1}) in a glass sheet (1.1×1.1 cm). After 24 h of incubation at 35 °C, the glass sheets were gently washed thrice with sterile 0.9% saline to remove the planktonic bacteria, then fixed, washed, dehydrated, and sputter-coated with gold before observation by SEM.

Protein Leakage Assay

To measure the leakage of proteins from bacterial cells, different volumes of LB medium, (1,4-DBTPP)Br_2, and MRSA cells were added to 20 mL cultures at a final concentration of 2 × MIC of (1,4-DBTPP)Br_2 and 1.0×10^9 CFU mL^{-1} of MRSA. Control groups were prepared without (1,4-DBTPP)Br_2. The mixture was incubated at 35 °C with shaking at 150 rpm. After 24 h, the sample was centrifuged at 10,000 rpm and 4 °C for 10 min. The supernatant was immediately collected, and the protein concentration of each sample was detected using a Bradford Protein Assay Kit (Beyotime, Nantong, China).[29]

Inhibition of Biofilm Formation

During the development of biofilms, MRSA cells were adjusted to McFarland Standard 0.5 (1.5×10^8 CFU mL^{-1}), (1,4-DBTPP)Br_2 was added (64 to 512 μg mL^{-1}) to the LB broth in 96-well microtiter plates (final bacterial concentration: 1.0×10^6 CFU mL^{-1}), and cells were incubated for 20 h at 35 °C. After incubation, each well was gently washed thrice with sterile 0.9% saline by removing the culture supernatant, then the adherent biofilm was fixed and stained with methanol (15 min) and 0.1% (wt/vol) crystal violet (5 min), respectively. Finally, the crystal violet was dissolved with the addition of 200 μL of ethanol (95%), and cell growth was assessed by measuring the value of OD_{595}, as previously reported.[30] In addition, (1,4-DBTPP)Br_2 was placed in polystyrene 24-well plates at graded concentrations (range 1/4–2 × MIC) in bacterial suspensions (1.0×10^6 CFU mL^{-1}) in LB broth. After a 48 h incubation, wells were rinsed thrice with a sterile 0.9% saline, and 0.01% final concentration of resazurin was added, followed by an incubation in the dark for 60 min. A microplate reader (Thermo Fisher Scientific, Waltham, MA, USA) was used to detect the optical density (OD_{570} and OD_{600}) values. Sterile saline solution (0.9% NaCl) was set as a negative control.[31]

In vitro Biocompatibility Evaluation

Cell Cytotoxicity Analysis

The cytotoxicity of (1,4-DBTPP)Br_2 against L929 cells was determined using a sensitive colorimetric assay of cell-counting kit-8 (CCK8, Yeasen Biotechnology, Shanghai). L929 cells were seeded into a 96-well plate at a density of 1.0×10^4 cells/well and cultured for 24 h. Cells were then treated with (1,4-DBTPP)Br_2 at various concentrations (0–128 μg mL^{-1}) for an additional 24 h. Then, 5 mg mL^{-1} of CCK-8 was added to each well, and the mixture was further incubated for 4 h at 37 °C and 5% CO_2. Subsequently, a microplate reader was used to detect the absorbance at 450 nm. Cell viability was calculated according to the following formula: Cell viability = (A_{450} of the treated group − A_{450} of blank control) / (A_{450} of negative control − A_{450} of blank control) × 100%.[32]

Hemocompatibility Test

We used a previously reported hemolysis assay to further evaluate blood compatibility.[33] The EDTA-stabilized blood from a female mouse was centrifuged at 1000 rpm for 10 min and washed thrice with phosphate-buffered saline (PBS) to remove the released hemoglobin. After removing the supernatant fraction, red blood cells (RBC) were resuspended (2% w/w) and placed in 5 mL centrifuge tubes, and RBC suspension (0.2 mL) was dispersed in (1,4-DBTPP)Br_2 (0.8 mL) at final concentrations ranging between 16 and 2048 μg mL^{-1}. PBS and 1% Triton were set as negative control (NC) and positive control (PC), respectively. Afterwards, each sample was incubated for 2 h at 37 °C, and centrifuged at 1000 rpm for 10 min, and then the supernatant (100 μL) was added into a 96-well plate and the value of OD_{540} was measured using a microplate reader. The hemolytic ratio (%) was calculated using the following formula:

Hemolysis ratio (%) = ($OD_{samples} - OD_{NC}$)/ ($OD_{PC} - OD_{NC}$).

In vivo Antibacterial and Wound Healing

All animal experiments were performed according to the research ethics committee of Fujian Medical University (2022-NSFC-0263). Two groups (n = 6) of Sprague Dawley (SD) rats (male, 180–200 g) were anesthetized with 2% pentobarbital sodium, and circular wounds (15 mm in diameter) were made on the dorsum of the rats. Then, the rats were infected by adding 200 μL of an MRSA suspension (1.5×10^8 CFU mL^{-1}) on the wounds. After a 24-h infection, 200 μL PBS or (1,4-DBTPP)Br_2 (640 μg mL^{-1}) was added to the infected areas for 24 h. Subsequently, the images of infected wounds were obtained, and their sizes were measured by a digital caliper.

Histological Analysis

At the end of the wound-healing experimental assay, the tissues of infected wounds and major organs (heart, liver, spleen, lung, and kidney) of the rats were fixed for 24 h in 4% paraformaldehyde. The tissues were prepared for hematoxylin and eosin (H&E) staining and Masson's trichrome (MT) staining, after desiccation with ethanol, embedding in paraffin, and cutting into slices (5 μm). The levels of tumor necrosis factor-α (TNF-α) and CD31 in the skin tissues of the wounded regions of mice were detected by immunohistochemical staining. CD68 expression was assessed by immunofluorescence

staining to determine the regulation of macrophage cells. The histochemical analysis results were further quantified by the ImageJ software. See Supporting Information for more details on methods.

Results and Discussion

Characterization of the Developed Quaternary Phosphorus Salts

Three different types of two alkyl-bis-(triphenyl)phosphonium bromides, (1,2-DBTPP)Br_2, (1,4-DBTPP)Br_2, and (1,6-DBTPP)Br_2, were synthesized using the one-step alkylation of triphenylphosphine with 1.2-dibromoethane. The products were characterized by FT-IR, UV-Vis, XRD, and NMR spectroscopies. In the FTIR analysis, the observed peaks were consistent with the characteristic vibrations of the $(1,2\text{-DBTPP})^{2+}$, $(1,4\text{-DBTPP})^{2+}$, and $(1,6\text{-DBTPP})^{2+}$ cations, For example, $\nu_{C\text{-}H}$ appear at around 3000 cm^{-1}, and $\gamma_{C\text{-}H}$ can be seen at round 680–870 cm^{-1}, specially, the $\nu_{C\text{-}P}$ can be monitored at 1110 cm^{-1} (Figure S1A). In the UV-Vis analysis, intense adsorption in the ultraviolet zone (214 and 270 nm) was assigned to the n–π*/π–π* transitions of the phenyl groups in the phosphonium core (Figure S1B). [34] Moreover, the XRD patterns suggested a crystalline phase (Figure S1C). As shown in Figure S2, ^1H NMR spectroscopy (500 MHz, Chloroform-d) for (1,4-DBTPP)Br_2 revealed the following: δ 7.94–7.87 (m, 12H), 7.75–7.71 (m, 6H), 7.68 (ddd, J = 8.6, 6.6, 3.4 Hz, 12H), and 4.03 (t, J = 14.7 Hz, 4H).

Antibacterial Activity of (1,4-DBTPP)Br_2

To measure the antibacterial activity of the quaternary phosphorus salts, four bacterial strains (*S. aureus*, MRSA, *E. coli*, and *P. aeruginosa*) were treated with the salts and their inhibition zone and MIC were evaluated. The agar diffusion assay showed that PA is insensitive to (1,2-DBTPP)Br_2, (1,4-DBTPP)Br_2, and (1,6-DBTPP)Br_2; however, the presence of a clear zone surrounding the well appeared where these three materials were introduced (Figure S3). The MIC values of the two alkyl-bis-(triphenyl) phosphonium bromides are shown in Table 1; (1,4-DBTPP)Br_2 showed better antimicrobial efficiency against MRSA than (1,2-DBTPP)Br_2 and (1,6-DBTPP)Br_2. Therefore, we focused on the antibacterial effect of only (1,4-DBTPP)Br_2 against MRSA in subsequent experiments. As shown in Figure 1A, 8 μg mL^{-1} (1/8 × MIC) to 64 μg mL^{-1} (1 × MIC) of (1,4-DBTPP)Br_2 significantly inhibited bacterial growth. A growth delay of 10 h occurred for MRSA when incubated with 32 μg mL^{-1} (1/2 × MIC) of (1,4-DBTPP)Br_2 at the onset of the logarithmic growth phase, termed the bacteriostatic effect.[35] Figure 1B shows that MRSA cells treated with 1, 2, and 4 × MIC of (1,4-DBTPP)Br_2 exhibited survival rates of 62.7%, 28.4%, and 8.4%, respectively, after 6 h of incubation. These results indicate that (1,4-DBTPP)Br_2 induces bacterial cell death in a dose-dependent manner, which was further confirmed by the gradually decreasing number of colonies grown on the LB plates, termed the bactericidal effect (Figure S4); (1,4-DBTPP)Br_2 induced nearly 90% cell death at high concentrations (4 × MIC). Collectively, these results indicate that (1,4-DBTPP)Br_2 exhibits strong antibacterial activity against MRSA.

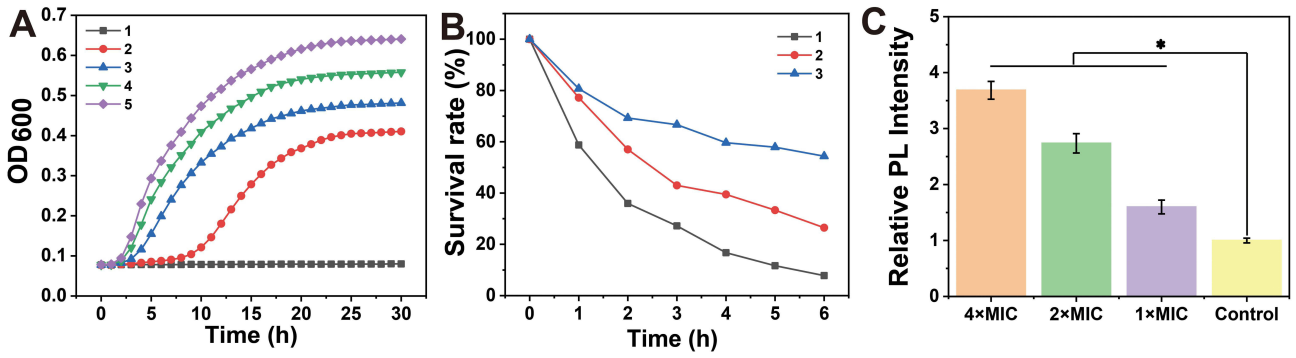

Figure 1 Antibacterial activity of (1,4-DBTPP)Br_2. (**A**) Growth curve of Methicillin-resistant *Staphylococcus aureus* (MRSA) after incubation with various concentrations of (1,4-DBTPP)Br_2 (1–5: 1, 1/2, 1/4, 1/8, and 0 × MIC). (**B**) Bacteria cell survival rate after incubation with various concentrations of (1,4-DBTPP)Br_2 (1–3: 4, 2, and 1 × MIC). (**C**) Relative fluorescence intensity of intracellular reactive oxygen species production level in MRSA treated with various concentrations of (1,4-DBTPP)Br_2 for 2 h. Data are means ± SD, n = 6, Student's *t*-test; * $p < 0.05$ compared to the PBS-treated group.

Table 1 Minimum Inhibitory Concentration (MIC) of (1,2-DBTPP)Br_2, (1,4-DBTPP)Br_2, and (1,6-DBTPP)Br_2, Towards Different Bacteria on the Basis of Different C Atoms

Strain	2C MIC (μg mL^{-1})	4C MIC (μg mL^{-1})	6C MIC (μg mL^{-1})
MRSA	≤128	≤64	≤128
SA	≤64	≤32	≤64
Ec	≤8000	≤8000	≤8000
PA	>64,000	>64,000	>64,000

Abbreviations: MRSA, Methicillin-resistant *Staphylococcus aureus*; SA, *Staphylococcus aureus*; Ec, *Escherichia coli*; PA, *Pseudomonas aeruginosa*.

Reactive Oxygen Species (ROS) Production and Destruction of the Bacterial Membrane

Many antibacterial materials promote ROS production, ultimately killing bacterial cells.[36] Wu et al reported the synergistic impacts of ROS and photothermal effects could kill bacteria rapidly and effectively.[37] Therefore, we investigated whether the antibacterial efficacy of (1,4-DBTPP)Br_2 was mediated by ROS production. As displayed in Figure 1C, the luminescence intensity of DCF was gradually enhanced (λex = 488 nm, λem = 522 nm) with the increase in (1,4-DBTPP)Br_2 concentrations, suggesting that (1,4-DBTPP)Br_2 promoted the production of intracellular ROS. This result indicates that at the early stage of exposure to (1,4-DBTPP)Br_2, bacteria may be exposed to high levels of ROS. Li et al also demonstrated the greater bactericidal efficiency towards *S. aureus* can be ascribed to the effect of ROS.[38]

To further elucidate the mechanism underlying the antibacterial effect of (1, 4-DBTPP) Br_2, we performed fluorescence imaging experiments using live/dead staining to investigate the integrity of the bacterial cell membrane.[39] SYTO 9 (green fluorescence) stains the nucleic acids of both live and dead bacteria whereas PI (red fluorescence) stains only dead bacteria with disrupted membranes. Fluorescent images of MRSA treated with PBS or (1,4-DBTPP)Br_2 are shown in Figure 2. For the bacteria treated with PBS, few red spots were observed whereas for the bacteria treated with (1,4-DBTPP)Br_2, a greater number of red spots was observed, further confirming the antibacterial effects of (1,4-DBTPP)Br_2 (Figure 2A and B). Moreover, we observed aggregates of dead bacteria in the fluorescent images of MRSA treated with (1,4-DBTPP)Br_2, a phenomenon similar to that reported for other materials.[40] Shen et al demonstrated that bacteria could

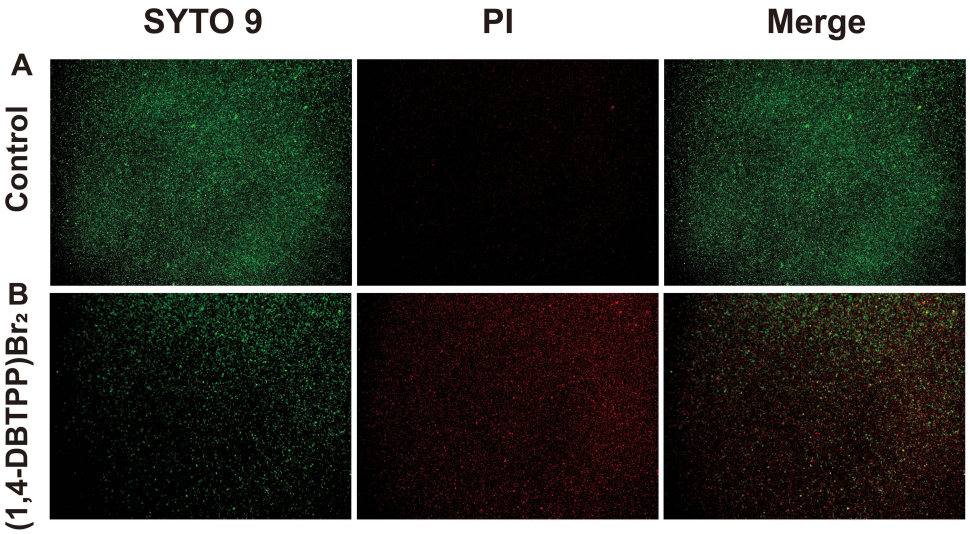

Figure 2 Fluorescent images of Methicillin-resistant *Staphylococcus aureus* (MRSA) treated with (**A**) phosphate-buffered saline or (**B**) (1,4-DBTPP)Br_2. Propidium iodide stains dead cells in red, and SYTO 9 stains both dead and living cells in green.

be captured and killed through effective interactions between nanomaterial and bacteria.[41] Furthermore, SEM was also used to observe (1,4-DBTPP)Br_2-induced morphological changes in the bacteria. As shown in Figure 3, PBS-treated MRSA cells were smooth and spherical whereas they exhibited loss of membrane integrity after the treatment of (1,4-DBTPP)Br_2. These results suggest that (1,4-DBTPP)Br_2 directly targets the cell wall or membrane of MRSA, causing cell damage and death by promoting the production of ROS.[42]

Wu et al developed a method for effective eliminating bacteria by destroying the bacterial outer membrane using microwaves.[43] Damage to the bacterial structure also leads to cytoplasm leakage. Therefore, we performed a quantitative protein leakage assay to confirm the destruction of the integrity of the membrane of MRSA by (1,4-DBTPP)Br_2. As shown in Figure 4A, the protein leakage in the (1,4-DBTPP)Br_2 group was approximately 4.5 times higher than that in the negative control (1.74 mg mL^{-1} vs 0.39 mg mL^{-1}). These results indicate that (1,4-DBTPP)Br_2 induces damage to bacterial cell integrity.

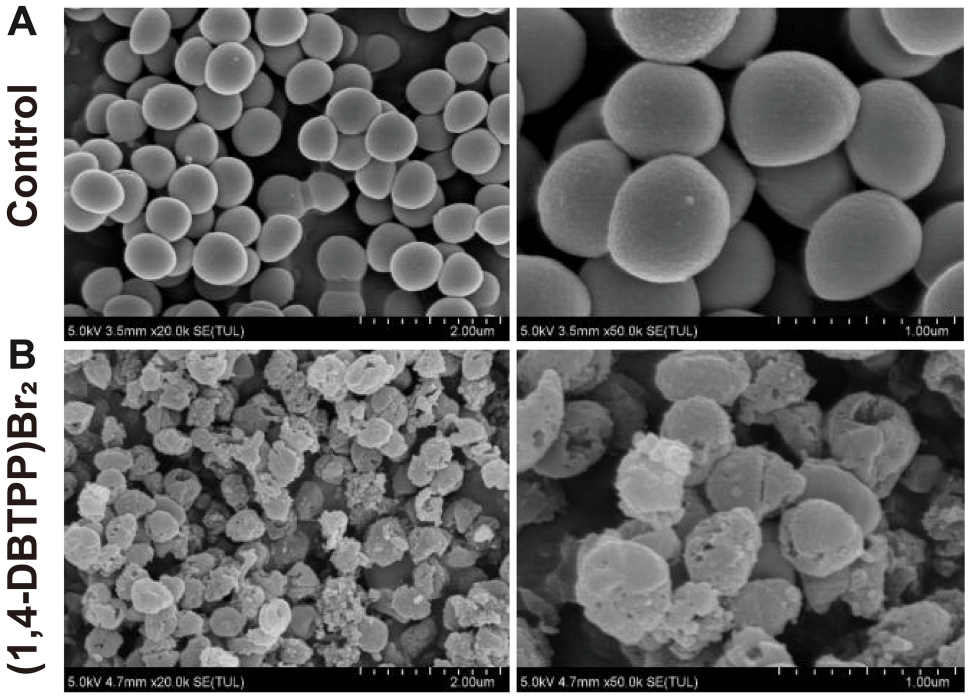

Figure 3 Scanning electron microscopy (SEM) images of Methicillin-resistant *Staphylococcus aureus* treated with (**A**) phosphate-buffered saline or (**B**) (1,4-DBTPP)Br_2 at 35 °C for 24 h.

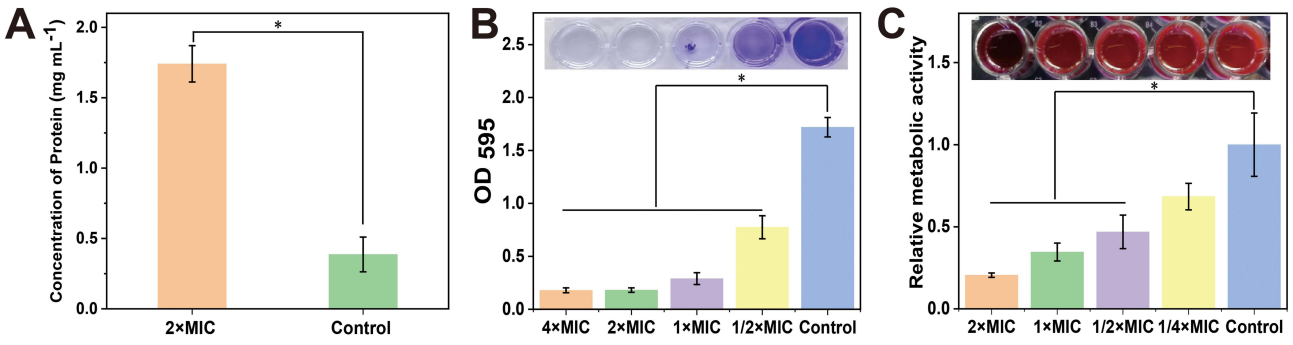

Figure 4 (**A**) Protein leakage from Methicillin-resistant *Staphylococcus aureus* (MRSA) suspensions treated with 2 × minimum inhibitory concentration (MIC) of (1,4-DBTPP)Br_2 for 2.5 h. Quantification and images (inset) of (1,4-DBTPP)Br_2 on MRSA biofilm formation after staining with (**B**) crystal violet and (**C**) resazurin (Excitation wavelength: 570 nm, Emission wavelength: 600 nm). Data are mean ± SD, n = 3, Student's *t*-test; * $p < 0.05$ compared to the PBS-treated group.

Biofilm Formation Inhibited by (1,4-DBTPP)Br_2

Bacterial biofilms are a significant cause of disease and drug resistance. Three-dimensional structures of bacterial biofilms are formed by embedding microbial clusters in a matrix of self-produced extracellular polymeric substances.[44,45] During the past years, various strategies have been designed to eliminate the formation of biofilms; however, the protection of these structures renders biofilms difficult to eradicate.[46] ROS exhibits excellent activity towards biofilm components, resulting in the oxidation of proteins, nucleic acids, as well as polysaccharides.[47] Hence, we explored the effects of (1,4-DBTPP)Br_2 on the inhibition of MRSA biofilm formation using crystal violet staining to measure the mass of biofilm. As displayed in Figure 4B, after the incubation of various concentrations of (1,4-DBTPP)Br_2 with the biofilm medium, the formation of MRSA biofilm was strongly inhibited with increasing amounts of (1,4-DBTPP)Br_2. Resazurin viability assay was used to measure the presence of active biofilm bacteria, which showed that the structures formed by MRSA on the plates were sensitive to (1,4-DBTPP)Br_2 (Figure 4C). Moreover, the metabolic activity of MRSA cells was significantly decreased by (1, 4-DBTPP)Br_2 in pre-grown structures; compared to the control group, treatment with 1/4–1/2 × MIC of (1,4-DBTPP)Br_2 caused a 30%–50% decrease in the metabolic activity of cultured MRSA whereas 1–2 × MIC of (1,4-DBTPP)Br_2 resulted in an 80% reduction in metabolic activity. Moreover, the adhesion of the MRSA biofilm on the glass surface was further observed using SEM.[48] As shown in Figure 5A, a considerable bacterial biofilm growth, which resulted in clusters with composite morphology, was visualized on the surface of the glass. In contrast, limited bacterial biofilm formation was observed on the surface of the (1,4-DBTPP)Br_2 treatment group (Figure 5B). These results indicate that (1,4-DBTPP)Br_2 can effectively prevent the formation of MRSA biofilms. In the future, further studies on the deeper understanding of antibacterial mechanisms should be evaluated.[49]

Cytotoxicity and Hemolysis Assay

To evaluate the potential toxicity of (1,4-DBTPP)Br_2, we investigated its effect on the viability of L929 cells using a CCK-8 kit. At 24 h of incubation, (1,4-DBTPP)Br_2 did not affect the cell viability (>90%) at concentrations ranging from 16 to 128 μg mL^{-1} (Figure 6A). Good biocompatibility of nanomaterial is necessary for applying in wound repair.[50]

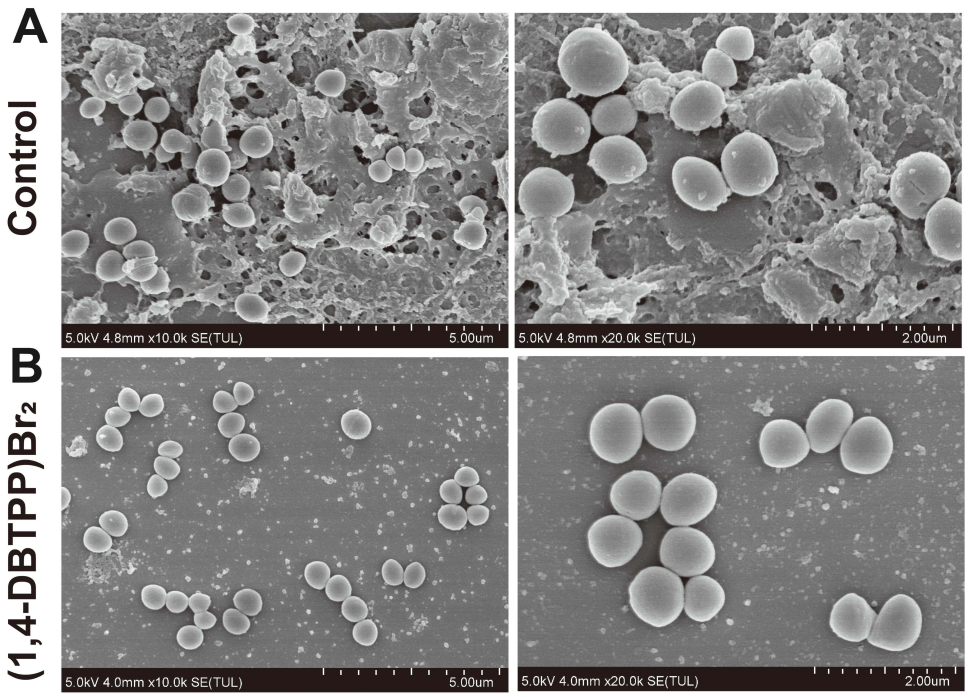

Figure 5 Scanning electron microscopy (SEM) images of biofilm formation of Methicillin-resistant *Staphylococcus aureus* (MRSA) treated with (**A**) phosphate-buffered saline or (**B**) (1,4-DBTPP)Br_2 at 35 °C for 24 h.

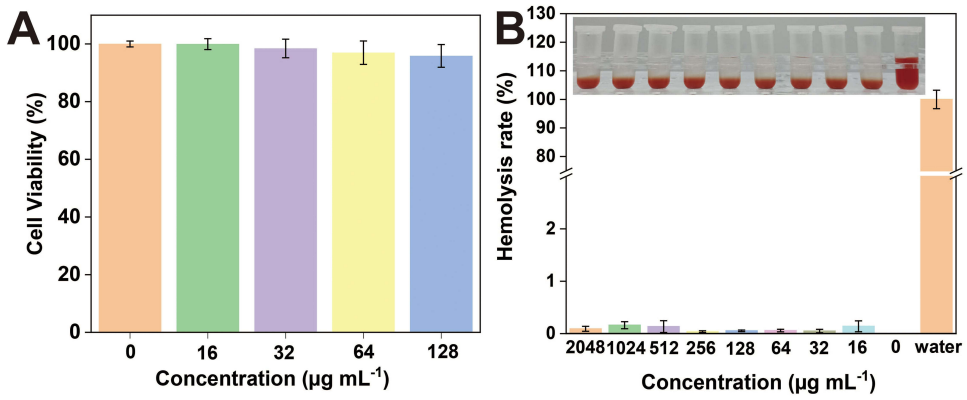

Figure 6 (**A**) Viability of L929 cells cultured with various concentrations of (1,4-DBTPP)Br_2 for 24 h. (**B**) Hemolysis activity of mouse blood treated with water and different concentrations of (1,4-DBTPP)Br_2 (0, 16, 32 64, 128, 256, 512, 1024, and 2048 μg mL^{-1}).

As hemolysis can hamper the application of (1,4-DBTPP)Br_2 in vivo, we further evaluated its blood compatibility.[51] After incubation with fresh mouse blood, (1,4-DBTPP)Br_2 at concentrations as high as 2048 μg mL^{-1} did not induce hemolysis (Figure 6B). These results demonstrate that (1,4-DBTPP)Br_2 exhibits excellent biocompatibility.

Healing of Infected Skin Wounds in vivo

To investigate the effect of (1,4-DBTPP)Br_2 on the healing of infected wounds in vivo, we randomly divided rats with MRSA-infected wounds into two groups. Figure 7A shows representative images of wound closure in rats treated with PBS or (1,4-

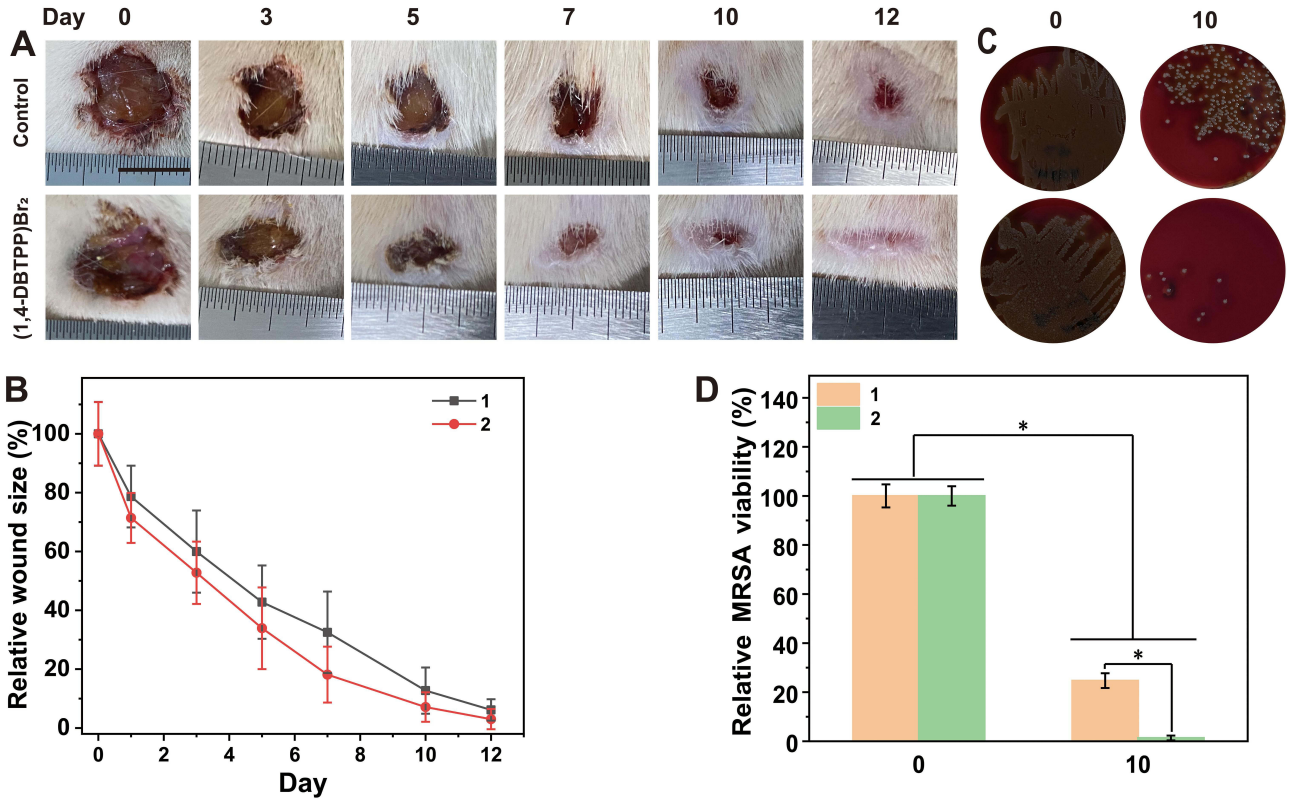

Figure 7 In vivo antibacterial activity of (1,4-DBTPP)Br_2. (**A**) Photographs of infected wounds. (**B**) Corresponding sizes (relative area versus initial area) of Methicillin-resistant *Staphylococcus aureus* (MRSA)-infected wounds after treatment with PBS or (1,4-DBTPP)Br_2, 1–2: control and (1,4-DBTPP)Br_2. (**C**) Images on bacterial clones on d 0 and 10 after treatment in vivo. (**D**) The corresponding quantitative results of the living clones cultured on the blood agar medium. 1–2: control and (1,4-DBTPP)Br_2. *$p < 0.05$.

DBTPP)Br_2 at different times (0, 3, 5, 7, 10, and 12 d). After treatment for 7 d, the area of infected wounds in the PBS and (1,4-DBTPP)Br_2 groups decreased to 32.5% and 18.1%, respectively, indicating that (1,4-DBTPP)Br_2 promoted wound healing (Figure 7B). To further investigate the antibacterial effect of (1,4-DBTPP)Br_2 in vivo, we assessed microbial clones on the wound tissues on days 0 and 10. The number of MRSA colonies continued to decrease over time (Figure 7C); on the 10th day, (1,4-DBTPP)Br_2-treated wounds produced drastically fewer bacterial colonies than the control group (Figure 7D). These results confirm the potent bactericidal activity of (1,4-DBTPP)Br_2 in the wound area.

The process of accumulation and activation is significant for inflammatory cells to transit from an inflammatory state to a wound-healing state. Therefore, we analyzed the inflammatory state of the wounds of the two groups using H&E staining. The results revealed that the amounts of inflammatory cells present on the wounds after treatment with (1,4-DBTPP)Br_2 was significantly lower than that present on the wounds treated with PBS (indicated by the orange arrow) (Figure 8A). Moreover, an intact epidermal layer (indicated by the black arrow) was found clearly in the (1,4-DBTPP)Br_2 group. In the control group, the incomplete epidermal layer was accompanied by obvious tissue damage (blue arrow). The statistical analysis of the skin thickness is shown in Figure 8C, in which the new epidermal layer of the (1,4-DBTPP)Br_2 group was thicker than that of the control group on day 12, indicating that (1,4-DBTPP)Br_2 accelerated wound healing and restored the defense function of normal skin.[52] Additionally, MT staining revealed that the (1,4-DBTPP)Br_2-treated wounds had increased collagen deposition (~78%) in the regenerated tissues, which was higher than that in the control group (Figure 8B and D). Moreover, H&E-stained pathological sections of the main organs (heart, liver, spleen, lung, and kidney) of the rats indicated no significant difference between the control and (1,4-DBTPP)Br_2-treated groups, suggesting that (1,4-DBTPP)Br_2 would not induce pathological damage to the rats (Figure S5). These results indicate that (1,4-DBTPP)Br_2 promotes wound healing.

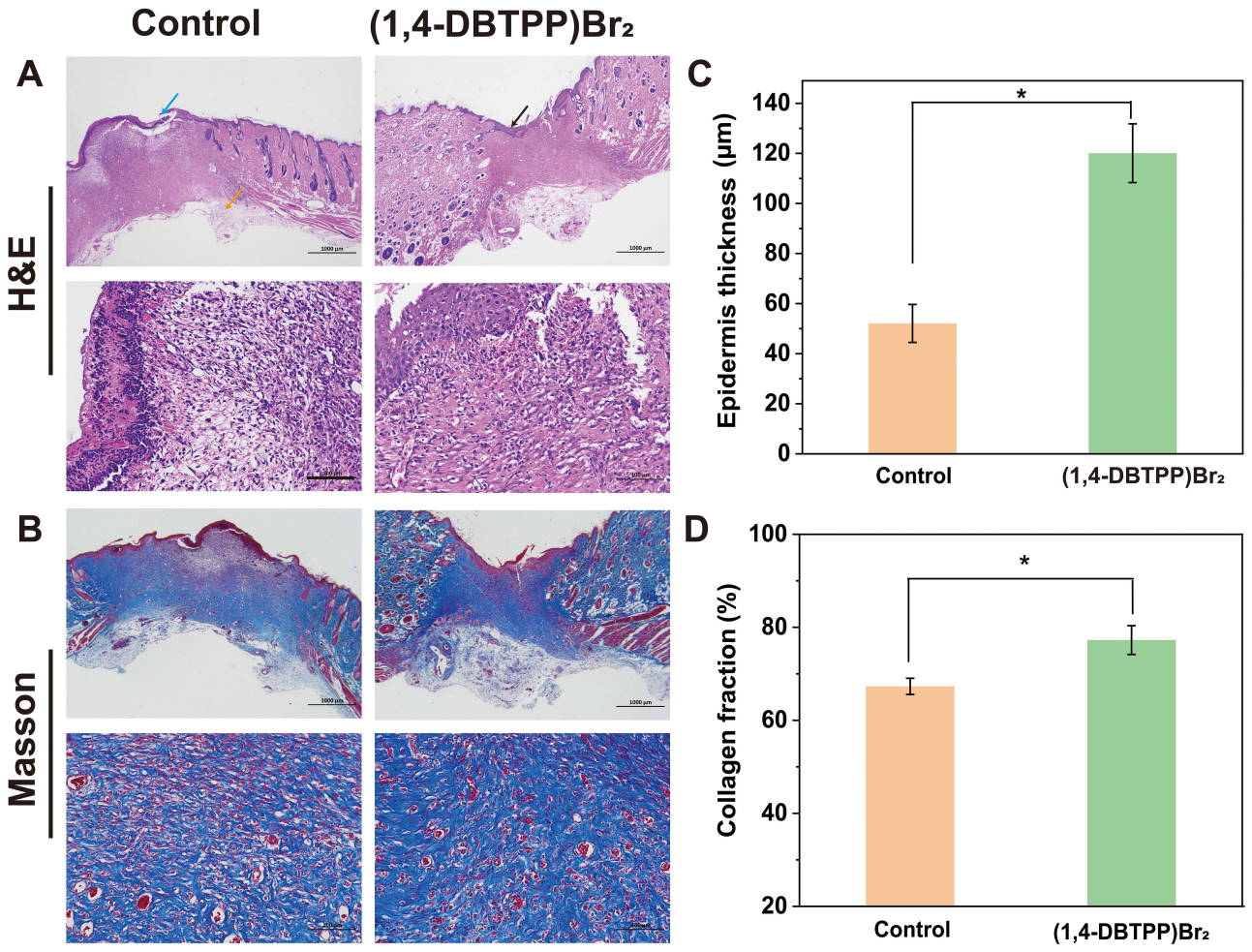

Figure 8 (**A**) Hematoxylin-eosin (H&E) staining and (**B**) Masson's trichrome (MT) staining images of infected wound tissue after various treatments for 12 d. (**C**) Thickness of newly formed epidermis (n = 3). (**D**) Collagen deposition on day 12 (n = 3), *$p < 0.05$.

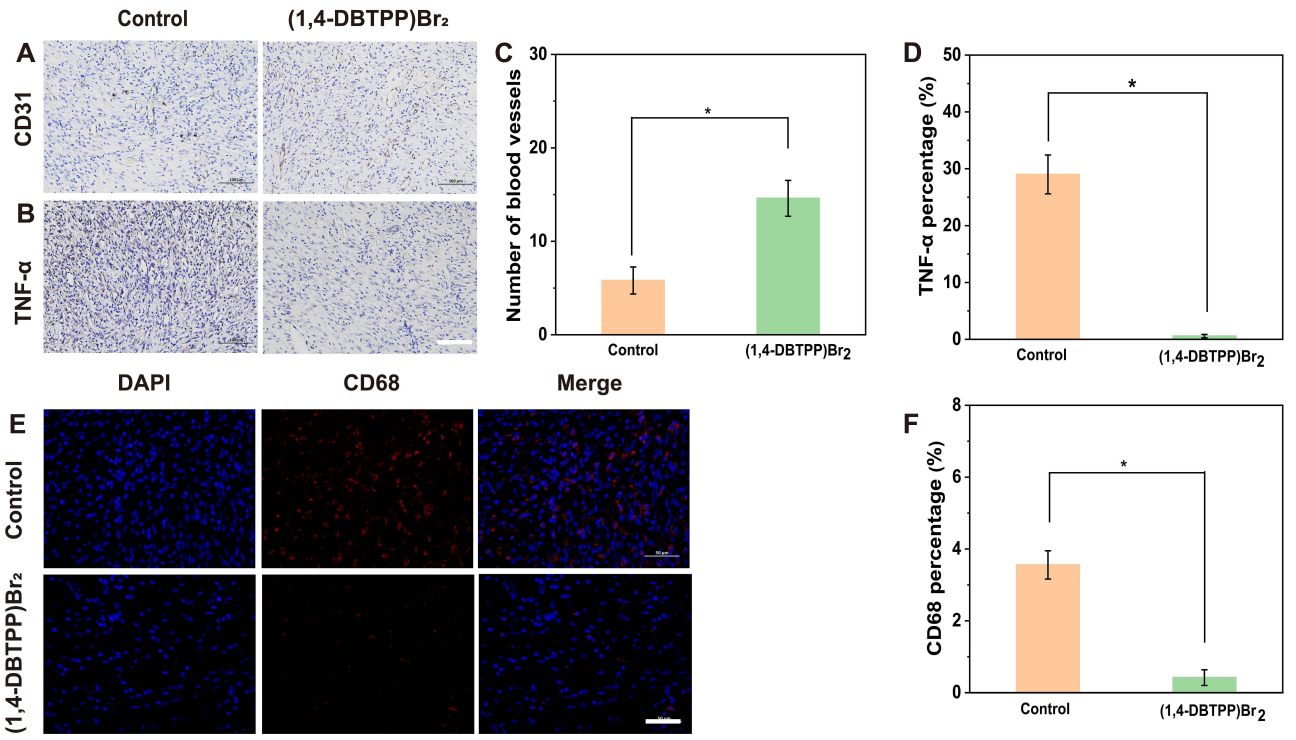

Figure 9 Immunohistochemical staining of (**A**) CD31 and (**B**) tumor necrosis factor (TNF)-α. Quantification of (**C**) blood vessels and (**D**) inflammatory area based on CD31 and TNF-α staining, respectively. Scale bar: 200 μm. (**E**) Immunofluorescence staining and (**F**) quantification percentage of CD68 cells on day 12. Scale bar: 50 μm. *$p < 0.05$.

Histological Analysis

To assess wound angiogenesis after treatment with (1,4-DBTPP)Br_2, we evaluated the level of the endothelial cell marker CD31.[53] As shown in Figure 9A, the wounds of the (1,4-DBTPP)Br_2 group had a large population of CD31+ cells compared to the control group. Furthermore, the newly formed blood vessels were counted based on CD31 staining, and the results showed that (1,4-DBTPP)Br_2 had a high number of blood vessels on day 12, which was 2.3-fold higher than that of the control group (Figure 9C). The (1,4-DBTPP)Br_2 group also had significantly decreased TNF-α expression, a marker of inflammation, compared to the control group (Figures 9B and D). These results indicate that (1,4-DBTPP)Br_2 exhibits excellent pro-angiogenic capabilities and anti-inflammatory properties during wound healing. Finally, immunofluorescence staining was used to demonstrate that the number of CD68+ cells in the (1,4-DBTPP)Br_2 group was greatly reduced on day 12 (Figure 9E and F), indicating a strong suppression of CD68 in MRSA infected wounds with (1,4-DBTPP)Br_2 treatment. Taken together, our results demonstrate that this novel material can reduce inflammatory response, stimulate the formation of new vessels, and enhance the deposition of collagen in vivo, thereby drastically accelerating wound healing.

Conclusions

In summary, we developed a novel phosphonium-based quaternary phosphorus salt (1,4-DBTPP)Br_2 with excellent antibacterial activity for the first time. This novel material exhibited potent antibacterial ability against MRSA cells and excellent hemocompatibility and nondetectable toxicity to mammalian cells. Moreover, (1,4-DBTPP)Br_2 prevented the formation of bacterial biofilms and disintegrated bacterial membranes and cell walls by promoting ROS production. Treatment with (1,4-DBTPP)Br_2 in vivo remarkably reduced abscesses in infected wounds, with no side effects on the major organs. Future studies on the optimal dosage of (1,4-DBTPP)Br_2 should be evaluated to facilitate its practical application. We believe that (1,4-DBTPP)Br_2 provides an effective platform for antimicrobial therapy.

Data Sharing Statement

The data of this article are included within the article and its Supplementary Document.

Funding

This work was financially supported by Joint Funds for the Innovation of Science and Technology of Fujian Province (2018Y9033; 2019Y9069), the Natural Science Foundation of Fujian Province (2022J01732), and Fujian Major Research Grants for Young and Middle-aged Health Professionals (2021ZQNZD015).

Disclosure

The authors declare no competing interest in this work.

References

1. Provenzani R, San-Martin-Galindo P, Hassan G, et al. Multisubstituted pyrimidines effectively inhibit bacterial growth and biofilm formation of *Staphylococcus aureus*. *Sci Rep*. 2021;11(1):7931. doi:10.1038/s41598-021-86852-5
2. Huh AJ, Kwon YJ. "Nanoantibiotics": a new paradigm for treating infectious diseases using nanomaterials in the antibiotics resistant era. *J Controlled Release*. 2011;156(2):128–145.
3. Hu DF, Li H, Wang BL. Surface-adaptive gold nanoparticles with effective adherence and enhanced photothermal ablation of methicillin-resistant *Staphylococcus aureus* biofilm. *ACS Nano*. 2017;11(9):9330–9339. doi:10.1021/acsnano.7b04731
4. Haidari H, Kopecki Z, Bright R, et al. Ultrasmall AgNP-impregnated biocompatible hydrogel with highly effective biofilm elimination properties. *ACS Appl Mater Interfaces*. 2020;12(37):41011–41025. doi:10.1021/acsami.0c09414
5. Zhao RT, Kong W, Sun MX, et al. Highly stable graphene-based nanocomposite (GO-PEI-Ag) with broad-spectrum, long-term antimicrobial activity and antibiofilm effects. *ACS Appl Mater Interfaces*. 2018;10(21):17617–17629. doi:10.1021/acsami.8b03185
6. Zhuang Y, Ren L, Zhang S, Wei X, Yang K, Dai K. Antibacterial effect of a copper-containing titanium alloy against implant-associated infection induced by methicillin-resistant *Staphylococcus aureus*. *Acta Biomater*. 2021;119:472–484. doi:10.1016/j.actbio.2020.10.026
7. Awasthi A, Sharma P, Jangir L, Kamakshi G, Awasthi KK, Awasthi K. Dose dependent enhanced antibacterial effects and reduced biofilm activity against Bacillus subtilis in presence of ZnO nanoparticles. *Mater Sci Eng C*. 2020;113:111021. doi:10.1016/j.msec.2020.111021
8. Nie L, Chang PB, Ji CC, et al. Poly(acrylic acid) capped iron oxide nanoparticles via ligand exchange with antibacterial properties for biofilm applications. *Colloids Surf B*. 2021;197:111385. doi:10.1016/j.colsurfb.2020.111385
9. Slavin YN, Asnis J, Häfeli UO, Bach H. Metal nanoparticles: understanding the mechanisms behind antibacterial activity. *J Nanobiotechnol*. 2017;15:65. doi:10.1186/s12951-017-0308-z
10. Huang H, Feng W, Chen Y, Shi J. Inorganic nanoparticles in clinical trials and translations. *Nano Today*. 2020;35:100972. doi:10.1016/j.nantod.2020.100972
11. Vimbela GV, Ngo SM, Fraze C, Yang L, Stout DA. Antibacterial properties and toxicity from metallic nanomaterials. *Int J Nanomedicine*. 2017;12:3941–3965. doi:10.2147/IJN.S134526
12. Han DL, Li Y, Liu XM, et al. Photothermy-strengthened photocatalytic activity of polydopamine-modified metal-organic frameworks for rapid therapy of bacteria-infected wounds. *J Mater Sci Technol*. 2021;62:83–95. doi:10.1016/j.jmst.2020.05.055
13. Han DL, Yu PL, Liu XM, Xu YD, Wu SL. Polydopamine modified CuS@HKUST for rapid sterilization through enhanced photothermal property and photocatalytic ability. *Rare Met*. 2022;41:663–672. doi:10.1007/s12598-021-01786-1
14. Han DL, Li Y, Liu XM, et al. Rapid bacteria trapping and killing of metal-organic frameworks strengthened photo-responsive hydrogel for rapid tissue repair of bacterial infected wounds. *Chem Eng J*. 2022;396:125194. doi:10.1016/j.cej.2020.125194
15. Han DL, Liu XM, Wu SL. Metal organic framework-based antibacterial agents and their underlying mechanisms. *Chem Soc Rev*. 2022;51:7138–7169. doi:10.1039/D2CS00460G
16. Jain A, Duvvuri LS, Farah S, Beyth N, Domb AJ, Khan W. Antimicrobial polymers. *Adv Healthcare Mater*. 2014;3(12):1969–1985. doi:10.1002/adhm.201400418
17. Ma Z, Wei DD, Yan P, Zhu X, Shan A, Bi ZP. Characterization of cell selectivity, physiological stability and endotoxin neutralization capabilities of α-helix-based peptide amphiphiles. *Biomaterials*. 2015;52:517–530. doi:10.1016/j.biomaterials.2015.02.063
18. Qin J, Guo JN, Xu QM, Zheng ZQ, Mao HL, Yan F. Synthesis of pyrrolidinium-type poly(ionic liquid) membranes for antibacterial applications. *Appl Mater Interfaces*. 2017;9(12):10504–10511. doi:10.1021/acsami.7b00387
19. Liu LH, Xu KJ, Wang HY, et al. Self-assembled cationic peptide nanoparticles as an efficient antimicrobial agent. *Nat Nanotechnol*. 2009;4(7):457–463. doi:10.1038/nnano.2009.153
20. Glukhov E, Stark M, Burrows LL, Deber CM. Basis for selectivity of cationic antimicrobial peptides for bacterial versus mammalian membranes. *J Biol Chem*. 2005;280:33960. doi:10.1074/jbc.M507042200
21. Marr AK, Gooderham WJ, Hancock REW. Antibacterial peptides for therapeutic use: obstacles and realistic outlook. *Curr Opin Pharmacol*. 2006;6(5):468–472. doi:10.1016/j.coph.2006.04.006
22. Xu H, Fang ZH, Tian WQ, et al. Green fabrication of amphiphilic quaternized β-chitin derivatives with excellent biocompatibility and antibacterial activities for wound healing. *Adv Mater*. 2018;30(29):1801100. doi:10.1002/adma.201801100
23. You SY, Huang YJ, Mao RT, et al. Together is better: poly(tannic acid) nanorods functionalized polysaccharide hydrogels for diabetic wound healing. *Ind Crops Prod*. 2022;186:115273. doi:10.1016/j.indcrop.2022.115273
24. Qi XL, Xiang YJ, Cai EY, et al. All-in-one: harnessing multifunctional injectable natural hydrogels for ordered therapy of bacteria-infected diabetic wounds. *Chem Eng J*. 2022;439:135691. doi:10.1016/j.cej.2022.135691
25. Ding BB, Gao HC, Song JH, et al. Tough and cell-compatible chitosan physical hydrogels for mouse bone mesenchymal stem cells in vitro. *ACS Appl Mater Interfaces*. 2016;8(30):19739–19746. doi:10.1021/acsami.6b05302

26. Patil RA, Talebi M, Xu C, Bhawal SS, Armstrong DW. Synthesis of thermally stable geminal dicationic ionic liquids and related ionic compounds: an examination of physicochemical properties by structural modification. *Chem Mater*. 2016;28(12):4315–4323. doi:10.1021/acs.chemmater.6b01247
27. Liu JB, Zhang QJ, Liu JZ, et al. Multifunctional quaternary phosphorus/bromoargentate hybrids: the achievement of greenish blue luminescence, repeatable photocurrent responses and durable antimicrobial activities with enhanced water stability. *Int J Nanomedicine*. 2020;15:6225–6237. doi:10.2147/IJN.S259156
28. Foerster S, Golparian D, Jacobsson S, et al. Genetic resistance determinants, in vitro time-kill curve analysis and pharmacodynamic functions for the novel topoisomerase II inhibitor ETX0914 (AZD0914) in *Neisseria gonorrhoeae*. *Front Microbiol*. 2015;10(6):1377.
29. Li WR, Xie XB, Shi QS, Zeng HY. Antibacterial activity and mechanism of silver nanoparticles on *Escherichia coli*. *Appl Microbiol Biotechnol*. 2010;85:1115–1122. doi:10.1007/s00253-009-2159-5
30. Zhang J, Kuang XY, Zhou YZ, Yang R, Xu X. Antimicrobial activities of a small molecule compound II-6s against oral *streptococci*. *J Oral Microbiol*. 2021;13(1):1909917. doi:10.1080/20002297.2021.1909917
31. Paduszynska MA, Maciejewska M, Greber KE, Sawicki W, Kamysz W. Antibacterial activities of lipopeptide $(C10)_2$-KKKK-NH_2 applied alone and in combination with lens liquids to fight biofilms formed on polystyrene surfaces and contact lenses. *Int J of Mol Sci*. 2019;20(2):393. doi:10.3390/ijms20020393
32. Zhou JL, Xiang HX, Zabihi F, Yu SL, Sun B, Zhu MF. Intriguing anti-superbug Cu2O@ZrP hybrid nanosheet with enhanced antibacterial performance and weak cytotoxicity. *Nano Res*. 2019;12:1453–1460. doi:10.1007/s12274-019-2406-8
33. Duan F. Feng Metalecarbenicillin framework-based nanoantibiotics with enhanced penetration and highly efficient inhibition of MRSA. *Biomaterials*. 2017;144:155–165. doi:10.1016/j.biomaterials.2017.08.024
34. Zhang WT, Liu JZ, Liu JB, et al. Quaternary phosphorus-induced iodocuprate(I)-based hybrids: water stabilities, tunable luminescences and photocurrent responses. *Eur J Inorg Chem*. 2018;2018(38):4234–4244. doi:10.1002/ejic.201800813
35. Chen JN, Peng H, Wang XP, Shao F, Yuan ZD, Han HY. Graphene oxide exhibits broad-spectrum antimicrobial activity against bacterial phytopathogens and fungal conidia by intertwining and membrane perturbation. *Nanoscale*. 2014;6:1879–1889. doi:10.1039/C3NR04941H
36. Liu SB, Zeng TH, Hofmann M, et al. Antibacterial activity of graphite, graphite oxide, graphene oxide, and reduced graphene oxide: membrane and oxidative stress. *ACS Nano*. 2011;5(9):6971–6980. doi:10.1021/nn202451x
37. Li JF, Li ZY, Liu XM, et al. Interfacial engineering of $Bi_2S_3/Ti_3C_2T_x$ MXene based on work function for rapid photo-excited bacteria-killing. *Nat Commun*. 2021;12:1224. doi:10.1038/s41467-021-21435-6
38. Li J, Song S, Meng JS, et al. 2D MOF periodontitis photodynamic ion therapy. *J Am Chem Soc*. 2021;143:15427–15439. doi:10.1021/jacs.1c07875
39. Yu SM, Li GW, Liu R, Ma D, Xue W. Dendritic Fe_3O_4@Poly(dopamine)@PAMAM nanocomposite as controllable NO-releasing material: a synergistic photothermal and NO antibacterial study. *Adv Funct Mater*. 2018;28(20):1707440. doi:10.1002/adfm.201707440
40. Park J, Kim J, Singha K, Han DK, Park H, Kim WJ. Nitric oxide integrated polyethylenimine-based tri-block copolymer for efficient antibacterial activity. *Biomaterials*. 2013;34(14):8766–8775. doi:10.1016/j.biomaterials.2013.07.064
41. Qi XL, Huang YJ, You SY, et al. Engineering robust Ag-decorated polydopamine nano-photothermal platforms to combat bacterial infection and prompt wound healing. *Adv Sci*. 2022;9:2106015. doi:10.1002/advs.202106015
42. Tao Y, Ju EG, Ren JS, Qu XG. Bifunctionalized mesoporous silica-supported gold nanoparticles: intrinsic oxidase and peroxidase catalytic activities for antibacterial applications. *Adv Mater*. 2015;27(6):1097–1104. doi:10.1002/adma.201405105
43. Qiao YQ, Xu YD, Liu XM, et al. Microwave assisted antibacterial action of Garcinia nanoparticles on Gram-negative bacteria. *Nat Commun*. 2022;13:2461. doi:10.1038/s41467-022-30125-w
44. Swartjes JJTM, Das T, Sharifi S, et al. A functional DNase I coating to prevent adhesion of bacteria and the formation of biofilm. *Adv Funct Mater*. 2013;23(22):2843–2849. doi:10.1002/adfm.201202927
45. García-Fernández L, Cui JX, Serrano C, et al. Antibacterial strategies from the sea: polymer-bound Cl-catechols for prevention of biofilm formation. *Adv Mater*. 2013;25(4):529–533. doi:10.1002/adma.201203362
46. Subbiahdoss G, Sharifi S, Grijpma DW, et al. Magnetic targeting of surface-modified superparamagnetic iron oxide nanoparticles yields antibacterial efficacy against biofilms of gentamicin-resistant staphylococci. *Acta Biomater*. 2012;8(6):2047–2055. doi:10.1016/j.actbio.2012.03.002
47. Zhuang QQ, Deng Q, He SB, et al. Bifunctional cupric oxide nanoparticle-catalyzed self-cascade oxidation reactions of ascorbic acid for bacterial killing and wound disinfection. *Composites, Part B*. 2021;222:109074. doi:10.1016/j.compositesb.2021.109074
48. Qu XH, Yang HT, Jia B, Yu ZF, Zheng YF, Dai KR. Biodegradable Zn–Cu alloys show antibacterial activity against MRSA bone infection by inhibiting pathogen adhesion and biofilm formation. *Acta Biomater*. 2020;117:400–417. doi:10.1016/j.actbio.2020.09.041
49. Fu JN, Zhu WD, Liu XM, et al. Self-activating anti-infection implant. *Nat Commun*. 2021;12:6907. doi:10.1038/s41467-021-27217-4
50. You SY, Xiang YJ, Qi XL, Mao RT, Cai EY. Harnessing a biopolymer hydrogel reinforced by copper/tannic acid nanosheets for treating bacteria-infected diabetic wounds. *Mater Today Adv*. 2022;15:100271. doi:10.1016/j.mtadv.2022.100271
51. Xie YZY, Zhang Q, Zheng WF, Jiang XY. Small molecule-capped gold nanoclusters for curing skin infections. *ACS Appl Mater Interfaces*. 2021;13(30):35306–35314. doi:10.1021/acsami.1c04944
52. Xie YJ, Yue LN, Zheng YD, et al. The antibacterial stability of poly(dopamine) in-situ reduction and chelation nano-Ag based on bacterial cellulose network template. *Appl Surf Sci*. 2019;491:383–394. doi:10.1016/j.apsusc.2019.06.096
53. Guo SC, Tao SC, Yin WJ, Qi X. Exosomes derived from platelet-rich plasma promote the reepithelization of chronic cutaneous wounds via activation of YAP in a diabetic rat model. *Theranostics*. 2017;7:81–96. doi:10.7150/thno.16803